Quantifying global aerosol direct radiative effect with MISR observations

Yang Chen
Qinbin Li
Ralph Kahn

Jet Propulsion Laboratory, California Institute of Technology, Pasadena, CA 91109

James Randerson

University of California, Irvine, CA 92697

Corresponding author: Y. Chen (Yang.Chen@jpl.nasa.gov)

Abstract

Using albedo, aerosol, cloud, and surface data from the Multi-angle Imaging SpectroRadiometer (MISR) instrument onboard the Terra satellite, the Short Wave Direct Radiative Effect (SWDRE) of aerosols was estimated for July 2002 on a global scale over both ocean and land. The critical step was deriving top of the atmosphere (TOA) broadband albedo in the absence of aerosols. Linear regressions between TOA broadband albedo and 0.56 μm aerosol optical depth (AOD) for different surface types were examined. MISR Photosynthetically Active Radiative integrated Bihemispherical Reflectance (BHRPAR) values were used to differentiate surface types. We find good correlations between TOA broadband albedo and AOD for 10°×5° grid cells. TOA albedo typically increases with increasing AOD for most regions, as expected, due to aerosol scattering. In the presence of absorbing aerosols, especially over biomass burning regions, the AOD-TOA albedo correlations produce much smaller (sometimes negative) slopes. The global pattern of cloud-free aerosol SWDRE is determined by the combined effects of aerosol loading, aerosol properties and surface types. The global mean value of cloud-free aerosol SWDRE derived for July 2002 is ~-4.7 W/m^2, consistent with prior satellite-based estimates. For the first time, we present an approach of estimating the aerosol SWDRE on a global scale based on satellite observations, over both ocean and land. Compared with the studies only over the ocean, this approach provides a more thorough representation of the climate effect due to aerosol scattering and absorption.

Key words: MISR, aerosol, radiative effect, satellite

1. Introduction

Aerosols, both natural and anthropogenic, can perturb the radiative balance of the Earth's atmosphere directly, by either scattering or absorbing the solar irradiance (Coakley et al., 1983; Chalson et al., 1990). The Short Wave Direct Radiative Effect (SWDRE) of aerosols has been estimated previously, using chemical transport and general circulation model simulations (e.g., Hansen et al., 1998). There are large uncertainties in these model estimates as well as discrepancies among them, due to incomplete knowledge of aerosol processes and assumptions made in the model aerosol simulations (Yu et al., 2006; Kinne et al., 2006; IPCC, 2001). Much effort has also been made to estimate aerosol radiative effects using measurements from ground based networks, satellite sensors, and intensive aircraft field experiments (e.g., Yu et al., 2006).

Satellite remote sensing provides frequent, global coverage of aerosol amount and type, as well as TOA radiance distribution, offering a unique opportunity for aerosol-related studies, including their effects on regional and global climate (Kaufman et al., 2002). Two approaches have been used previously to exploit satellite data in the calculation of aerosol SWDRE. In the first approach, satellite aerosol observations are input to a radiative transfer model, and the aerosol radiative effect is then derived from the radiative transfer calculation (Yu et al., 2004; Bellouin et al., 2005; Remer and Kaufman, 2006). The second approach uses satellite observations directly, without resorting to a radiative transfer calculation. In this case, the aerosol direct radiative effect is derived from the change of measured broadband radiative flux when aerosols are present in the atmosphere (Christopher et al., 2000; Loeb and Kato, 2002; Christopher and Zhang, 2002; Loeb and

Manalo-Smith, 2005). The latter approach requires fewer assumptions about aerosol microphysical properties.

In most previous studies using the satellite-only approach (Christopher et al., 2000; Loeb and Kato, 2002; Christopher and Zhang, 2002), the Clouds and the Earth's Radiant Energy System (CERES) broadband radiative observations (Wielicki et al., 1996) were used. The CERES radiance has coarse spatial resolution (~20km) and the results may have biases when omitting the radiative effect in partly cloudy grid cells. The coarse spatial resolution also makes cloud filtering difficult. Loeb and Manalo-Smith (2005) converted Moderate Resolution Imaging Spectroradiometer (MODIS) spectral radiances to broadband short wave radiances using a relationship derived from concurrent measurements of MODIS spectral and CERES broadband radiances. The resulting broadband radiances were then used to estimate top of the atmosphere (TOA) radiative fluxes using an angular distribution model (ADM). Because of the finer resolution of the MODIS footprint, this method reduces the bias due to partial cloud cover.

However, to our knowledge, the satellite-only approach has so far only been used over the ocean. It is still challenging to estimate the aerosol SWDRE over land from satellite observations, mainly due to the large uncertainty in retrieving aerosols over land surfaces and the difficulty to estimate the TOA radiative flux for aerosol-free scenes (Loeb and Kato, 2002).

The Multi-angle Imaging SpectroRadiometer (MISR) aboard NASA's Terra satellite provides more accurate aerosol property retrievals over land with multi-angle information than single-angle, multi-spectral techniques (Abdou et al., 2005). In this study we present a method in which the aerosol properties, TOA albedo, and surface properties from MISR observations are used to estimate the aerosol SWDRE on a global scale over both ocean

and land. In this method, correlations between the TOA broadband albedo and 0.56 μm Aerosol Optical Depth (AOD) are investigated for different regions, and for different surface types within a region. We also study how aerosol SWDRE is affected by aerosol properties and surface type. Detailed descriptions of the data and method used in calculating aerosol SWDRE are presented in section 2. The results of AOD-TOA albedo correlations and global aerosol SWDRE distribution are shown in section 3. Conclusions are given in section 4.

2. Data and Methodology

2.1. MISR observations

The MISR sensor uses nine cameras pointed at fixed viewing angles (0º, ±26.1º, ±45.6º, ±60.0º, ±70.5º) to observe reflected and scattered sunlight in four spectral bands, nearly simultaneously (Diner et al., 1998). The four bands are centered at 446 (blue), 558 (green), 672 (red), and 866 nm (near infrared, NIR). The swath width is ~360km, which provides global coverage in about 9 days at the equator and 2 days near the poles.

MISR global retrievals of aerosols, TOA albedo, surface properties and cloud information are available for the period beginning in late February 2000. Each orbit is divided into 180 uniformly-sized blocks. Each block is 563.2 km (cross-track) × 140.8 km (along-track) in size. Since earth's surface has complex features such as topography, the synergistic use of multi-angle information from MISR enables us to better capture the links between structure and radiation, as well as their climatic and environmental effects (Diner et al., 2005). Specifically, with good-quality retrievals, MISR provides a unique

opportunity to study aerosol perturbations on the radiative balance of the atmosphere. We use multiple MISR level 2 products in this study.

The aerosol SWDRE is manifested by a change of TOA albedo due to the presence of aerosols. Several albedo products are generated from the MISR TOA radiances (Diner et al., 1999a). The MISR spectral TOA local albedo level 2 product is used to compute the TOA broadband albedo for the present study (detailed procedures are given in section 2.2). The MISR TOA local albedo is assessed from the elevation of maximum observed brightness contrast, called the Reflecting Layer Reference Altitude (RLRA), determined from the multi-angle data for every 2.2 × 2.2 km^2 pixel. The RLRA surface can jump discontinuously from pixel to pixel, so light emanating from one pixel may be obstructed by a higher nearby pixel on its way to the top of the atmosphere. The local TOA albedo is defined for a given 2.2 × 2.2 km^2 pixel as the ratio of unobstructed upwelling irradiance through the RLRA to the downwelling TOA irradiance above the RLRA. This is the highest spatial resolution albedo product produced from the MISR data, and it accounts for the top-leaving, but not the side-leaving, radiation from each pixel. The side-leaving radiance is stored separately in the MISR product. The maturity level of the MISR TOA Local Albedo product (Version 8) is Stage 1 Validated, i.e., product uncertainties have been estimated from independent measurements at selected locations and times (Loeb and Sun, 2006; Bull et al., 2005).

Using its multi-angle and multi-spectral observations, MISR is able to retrieve some information about aerosol size, shape, and single-scattering albedo, in addition to optical depth, over dark water and heterogeneous land (e.g., Martonchik et al., 2002; Kahn et al., 2001; 2005; Kalashnikova and Kahn, 2006; Chen et al., 2007). The Level 2 Aerosol Product has a spatial resolution of 17.6 × 17.6 km^2 (Diner et al., 2001a). MISR mid-

visible AOD (Version 16 and above) over heterogeneous surfaces and dark water has been Stage 2 validated, i.e., uncertainties are estimated from widely distributed, independent measurements (Kahn et al., 2005; Bull et al., 2005). The MISR Level 2 AOD data used in this study are Version 19.

The MISR retrievals also provide a number of parameters related to land surface properties. We use in this study the Photosynthetically Active Radiative integrated Bihemispherical Reflectance (BHRPAR) to differentiate land surface types (Martonchik et al., 1998). BHRPAR represents the bihemispherical, angular-integrated and spectral-integrated surface reflectance under ambient illumination conditions. We selected this rather than the Bihemispherical Reflectance (BHR) or the Directional Hemispherical Reflectance (DHR). The PAR band covers the 400-700 nm wavelength range, which includes three of the four MISR channels in the integration rather than just one (Schaepman-Strub et al., 2006; Diner et al., 1999b), making it especially well suited to categorize different surface types for the purpose of deriving AOD-TOA albedo correlations. The performance of MISR land surface parameters in classifying vegetation and other surface types has been widely evaluated (e.g., Hu et al., 2007; Armston et al., 2007). The MISR BHRPAR data (Version 19) has a spatial resolution of 2.2×2.2 km^2.

Mazzoni et al. (2006) recently developed scene classifiers, reported for each MISR 1.1×1.1 km^2 pixel using Support Vector Machine (SVM) techniques. The SVM scene classification is used operationally in the newest MISR data processing (Bull et al., 2005). The principal classifier identifies pixels as belonging to one of five groups: Clouds, Aerosols, Ice/Snow, Water and Land. Compared with classification by human experts, the accuracy of the SVM scene classifier is approximately 81% globally at the 1.1-km

pixel level (Mazzoni et al., 2006). In this study, the MISR SVM scene classifier product is used to set cloud mask for the purpose of reducing cloud contamination.

2.2. Method

We estimate the aerosol SWDRE by examining the change of TOA broadband albedo due to the presence of aerosols. We focus our analysis on July 2002. The same analysis will be applied to other months and years in future work.

As introduced above, different MISR level 2 data products often have different spatial resolutions. In the analysis presented here, we will refer to 10º (longitude) × 5º (latitude) grid boxes as 'regions', 1º×1º grid boxes as 'grids', 17.6×17.6 km^2 grid boxes as 'areas', and 2.2×2.2 km^2 and 1.1×1.1 km^2 boxes shown in MISR images as 'pixels', for the sake of convenience. The monthly mean TOA broadband albedo in the absence of aerosols is calculated for each 2.2×2.2 km^2 pixel, then averaged onto 1º×1º grids. The cloud-free aerosol radiative effect $\Delta F_{cloud-free}$ for each grid is then derived as follows:

$$\Delta F_{cloud-free} = I_{TOA}\left(\alpha_{with\_aerosol} - \alpha_{no\_aerosol}\right) \quad (1)$$

where I_{TOA} is the TOA incoming solar radiative flux (W/m^2) and $\alpha_{with\_aerosol}$ and $\alpha_{no\_aerosol}$ are the TOA broadband albedos with and without aerosols present.

We assume the aerosol radiative effect in cloudy regions is negligible and estimate the all-sky aerosol SWDRE $\Delta F_{all-sky}$ as follows:

$$\Delta F_{all-sky} = \Delta F_{cloud-free} \times \left(1 - CF\right) \quad (2)$$

where *CF* is the cloud fraction. As Loeb and Manalo-Smith (2005) pointed out, this approach ignores aerosols above cloud layers, which may overestimate the radiative cooling effect of aerosols in polluted regions (Ackerman et al., 2000).

A schematic flowchart of the abovementioned approach is shown in Figure 1. Several steps are taken to derive the mean TOA broadband albedo in each 1º×1º grid. First, by filling the missing side-leaving Bidirectional Reflectance Factors (BRF) and doing the angular integration, we calculate the total TOA spectral albedo that includes the side contributions. As mentioned above, during the processing of Level 2 MISR albedo data, the Level 1B2 ellipsoid-projected radiances were converted to BRFs and re-projected onto the RLRA (Diner et al., 1999a). The re-projection results in all measured BRFs being attributed to either an RLRA surface at the top of a column (top-leaving BRFs), or to the sides of a column (side-leaving BRFs). The TOA local albedos from the MISR Level 2 standard products are determined entirely from the top-leaving BRFs, while the side-leaving BRFs are left out of this product. Using only these albedos would probably cause an underestimation of the aerosol radiative effect. So in this study, we use two MISR level 2 parameters (mean side-leaving BRFs and the number of unobscured pixels on the sides of RLRA columns) to estimate the side contribution to TOA albedo for each 2.2×2.2 km^2 pixel. The unobscured side-leaving BRFs from different cameras are weighted using pre-established solid angle weighting factors (Diner et al., 1999a). The final total TOA spectral albedo is the sum of TOA local albedo from the MISR standard product and the contribution from side-leaving BRFs.

In order to calculate the aerosol radiative effect, it is necessary to convert the spectral albedos to broadband albedo. We convert the spectral TOA Local Albedos (which include the side-leaving contribution) to broadband albedo following Sun et al. (2006). In

this approach, for each viewing direction, MISR spectral reflectances in the red and NIR bands are related to CERE short wave broadband reflectance as given in Loeb et al. (2006). Reflectances at view and azimuth angles not sampled by MISR are extrapolated using a radiative transfer code applied to a plane parallel cloud model. The angular integration over these angles produces regression coefficients dependent only on solar zenith angle. Based on calculations using these coefficients, Sun et al. (2006) showed that the relative differences and relative root mean square (RMS) differences between MISR and CERES broadband albedos are ~0.8% and ~4.3%, respectively, for 1° x 1° overcast scenes over ocean. We use here the coefficients derived by Sun et al. (2006) to convert the MISR spectral TOA albedos to broadband TOA albedo.

Clouds may oftentimes contaminate satellite retrievals of aerosol and surface properties. The cloud mask is thus used to screen out cloudy areas and reduce cloud contamination. The cloud mask is also needed to calculate the all-sky aerosol radiative effect (see equation 2 and Figure 1). The MISR SVM Scene Classifiers provide four confidence levels of cloud presence: 'highly likely', 'likely', 'unlikely', and 'highly unlikely' for each 1.1×1.1 km^2 pixel. To reduce cloud contamination, we assume, conservatively, that a 17.6×17.6 km^2 area is 'cloudy' if a single 1.1×1.1 km^2 pixel within it has a cloud confidence level of 'highly likely' or 'likely'. These 'cloudy' areas are then excluded in further calculations.

2.3. TOA albedo in the absence of aerosols

The key step in our derivation of aerosol SWDRE is to estimate the aerosol-free TOA albedo, $\alpha_{no\_aerosol}$. One approach to quantifying $\alpha_{no\_aerosol}$ is to examine the correlation

between TOA albedo and AOD. Loeb and Kato (2002) examined the linear regression between TOA albedo from CERES and 0.63 μm AODs from the visible infrared scanner (VIRS) over tropical oceans for various SZAs. The y-intercept (zero AOD) was then an estimate of $\alpha_{no\_aerosol}$. Another way to estimate $\alpha_{no\_aerosol}$ is to do a radiative transfer calculation of the atmosphere in the absence of aerosols (Remer and Kaufman, 2006). Assumptions on surface albedo and trace gases concentrations are needed in such a calculation. In this study, we chose the former approach in consideration of the internal consistency between the calculation of TOA albedos with and without the presence of aerosols. This consistency is important because the aerosol radiative effect is derived from the difference between $\alpha_{with\_aerosol}$ and $\alpha_{no\_aerosol}$. In the latter approach mentioned above, abnormal values of aerosol SWDRE may occur due to the different methods in estimating $\alpha_{with\_aerosol}$ and $\alpha_{no\_aerosol}$.

In order to get better correlations between AOD and TOA albedo, we improve upon the Loeb and Kato (2002) approach as follows. First, Loeb and Kato (2002) did not consider the spatial variability of surface and aerosol types. We instead examine the AOD-TOA albedo regression for each 10°×5° region. To do this, we first calculate the mean values of TOA broadband albedo and 0.56 μm AOD from MISR observations for each 17.6×17.6 km^2 area. We then do the linear regression based on all available AOD-TOA albedo data pairs in each 10°×5° region during a month. Such spatial resolution, as shown in section 3.2, provides enough data for statistical analysis, allowing for linear regressions in most regions. Second, we use MISR BHRPAR data to differentiate land surface types in our regression analysis. This can reduce the uncertainty in aerosol SWDRE estimation induced by surface heterogeneity. Based on the global probability

distribution of BHRPAR values (Figure 3d), we use 26 bins of BHRPAR values to represent different surface types.

Over remote oceans, aerosol loading is generally too low to produce a meaningful linear regression between TOA albedo and AOD. This is due to the small dynamic range of AOD, and that the MISR aerosol retrieval at very small AOD is less reliable in a relative sense (Diner et al., 2001a; Kahn et al., 2005). In such cases, in order to increase the AOD dynamic range, the data used for AOD-TOA albedo regression are not limited to 10°×5° regions. Instead we do the regression for the global oceanic regions. Additionally, considering that the aerosol effects on TOA albedo are partly determined by the SZA, we derive the separate $\alpha_{\text{no aerosol}}$ values for different SZA bins, following Loeb and Kato (2002). Figure 2(a) shows the dependence of the $\alpha_{\text{no aerosol}}$ value on SZA based on the MISR data. This dependence is small when the SZA is less than 40˚, and increases gradually for larger SZAs. This pattern is similar to that in Loeb and Kato (2002), which was derived from the regressions of TOA fluxes from CERES and VIRS 0.63 μm AOD. The slope of the TOA albedo vs AOD curve, plotted in Figure 2(b) as a function of SZA, reflects the efficiency with which aerosols impact the TOA albedo. The value increases when SZA increases, and the large scatter at high SZA indicates higher sensitivity to differences in both aerosol amount and type over the ocean.

3. Results and discussion

3.1. Global distributions of AOD, TOA albedo, and BHRPAR

Figures 3(a) and 3(b) show monthly mean values of MISR-retrieved 0.56 μm AOD and TOA broadband albedo (including side contributions, see section 2.2) for July 2002.

These values are only for conditions with cloudy scenes filtered out. The SZA at MISR overpass time varies with latitude, and on July its lowest value occurs around 15°N. Since MISR aerosol retrievals at very large SZAs are of low quality (Diner et al., 2001a), we only show (and use) the values for regions between 30°S and 60°N, where the SZA is smaller. High AOD values are seen in desert regions such as the Sahara and the Arabian Peninsula, in anthropogenic aerosol source regions such as South and East Asia, Eastern Europe, North America, and in biomass burning regions such as Central Africa. Outflow of dust aerosols from the Sahara and biomass burning aerosols from Central Africa to the Atlantic is evident. Higher aerosol loadings are also seen over the adjacent oceans near the eastern US coast, and the coasts of South and East Asia. Over South America, frequent cloud cover masks the significant biomass burning aerosols produced in this area. TOA albedo is affected by aerosols, but is not solely determined by AOD. It also depends on other parameters such as surface reflectivity (Liang et al., 1999). The BHRPAR data shown in Figure 3(c) indicates that land surface is very heterogeneous in reflecting solar radiation. Most BHRPAR values over land are in the range of 0-0.4. Based on the probability distribution of the BHRPAR values (Figure 3(d)), we divided the land surface into 26 bins (10 bins with BHRPAR between 0 and 0.1, 15 bins between 0.1 and 0.4, and 1 bin above 0.4). We examine the AOD-TOA albedo regression for each BHRPAR bin in every 10°×5° region over land.

3.2. Correlation between TOA broadband albedo and 0.56 μm AOD

Figures 5 and 6 show the correlations between TOA broadband albedo and 0.56 μm AOD at representative sites shown in Figure 4 over the ocean and land, respectively. The

correlation varies for different regions due to different aerosol properties, surface types, and different retrieval uncertainties. We found linear correlations between TOA albedo and AOD for most 10°×5° regions over both ocean and land. We consider a linear regression successful if the RMS error of the regression is smaller than a preset value which is a function of BHRPAR, and if there is a large enough AOD dynamic range.

Over the ocean, $\alpha_{\text{no aerosol}}$ is relatively uniform. Most oceanic regions show $\alpha_{\text{no aerosol}}$ between 0.06 and 0.07. TOA albedo generally increases with increasing AOD value, reflecting the scattering from aerosols that increases the reflectivity of the atmosphere. Atmospheric temperature will decrease as AOD increases under these conditions, except possibly in any absorbing aerosol layers, because aerosol scattering brightens the scene over a dark ocean surface (Charlson et al., 1990). The Central Africa Coast region ((f) in Figures 4 and 5) shows large $\alpha_{\text{no aerosol}}$, which is likely due to the large SZA there. The difference of AOD dynamic range between scattering aerosols and absorbing aerosols (i.e., more absorbing aerosols produce a high AOD range when biomass burning effects are large) may also affect the linear regression and cause large $\alpha_{\text{no aerosol}}$ in this region. The slope of the AOD-TOA albedo correlation represents the ability of aerosols to modify the planetary albedo. Since the deep ocean surface is relatively homogeneous, this slope is affected mainly by aerosol properties. The AOD distributions and slopes of AOD-TOA albedo for the Eastern US Coast (region (a)) and East Asia Coast (region (d)) are very similar, probably reflecting similar anthropogenic sources of aerosols in these regions at this month. In the regions where biomass burning is the main aerosol source, such as in Central Africa (region (f)), the rate of change of TOA albedo due to aerosols is smaller. This is likely due to absorbing (mainly carbonaceous) aerosols from biomass burning, that generally have smaller single scattering albedos than desert dust or even

industrial pollution, especially near the sources. The absorption of solar radiation diminishes the effect of aerosol scattering on upwelling radiation, lowering the slope of the AOD-TOA albedo correlation. The West Africa Coast (region (b)) represents a typical dust aerosol scenario, where high AOD values can be found in spring and summer. The Arabian Sea (region (c)) has seasonally reversing monsoons from winter to summer (Rudnick et al., 1997). In July, the prevailing southwest wind transports both dust particles from the desert and biomass burning aerosols from Central Africa to this region. The resulting slope lies between that of the dust dominated region (b) and the biomass burning aerosol dominated region (f).

As mentioned above, in addition to the 10°×5° regional divisions, over land we also divide each region into different surface types according to the mean BHRPAR values. Figure 6 shows the correlations of AOD-TOA albedo at three regions over land representing typical aerosol types, each stratified by BHRPAR. In the Eastern US (region (A)), most BHRPAR values are between 0.03 and 0.09, AOD ranges from 0.05 to 0.6, and medium, spherical, weakly or non-absorbing anthropogenic aerosols are dominant. The correlations between TOA albedo and AOD are very good for most BHRPAR bins (RMS < 0.02). The slope decreases as BHRPAR increases. This indicates that when the surface is brighter (more reflective), other things being equal, the aerosol scattering effect on planetary albedo is smaller. Most points in Central Africa (region (B)) have BHRPAR between 0.03 and 0.12, similar to that in the Eastern US (region (A)). However, the slopes for Central Africa are smaller than those for the Eastern US. For some BHRPAR bins, the slope is even negative, which means increased aerosol correlates with decreased TOA albedo, corresponding to probable aerosol warming effect (e.g., Menon et al., 2002). This is likely due to light absorption by darker biomass burning particles, similar to the

situation over the ocean near the Central Africa Coast (region (f)). Compared with the Central Africa Coast, the slopes over land for Central Africa are even smaller, because the land surface is more reflective, reducing the scattering contribution of superposed aerosols. The Saharan Desert (region (C)) has very large AOD values, and most data points in this region have much larger BHRPAR values due to low vegetation coverage. Similar to the Eastern US (region (A)), TOA albedo in the Saharan Desert region increases as AOD increases, and the slope becomes smaller for larger BHRPAR values. However, the relationship between TOA albedo and AOD is very scattered, which can be attributed to large AOD variability, and corresponding uncertainty in MISR aerosol retrievals in this region. The large reflectivity of the desert surface contributes to this uncertainty, by producing a large radiance signal that competes with the atmospheric aerosol signal at the TOA.

3.3. Shortwave direct radiative effect of aerosols

Based on the mean TOA broadband albedo in the presence and absence of aerosols (section 3.2), we calculate the cloud-free aerosol SWDRE from Equation (1). We take all available cloud-free cases at MISR overpass time (10:30am local time) during July 2002 and calculate the monthly mean value for each 1°×1° grid cell. Figure 7(a) shows the monthly mean value of cloud-free aerosol SWDRE for July 2002. The SWDRE pattern over the ocean is similar to the 0.56 μm AOD pattern from MISR, as shown in Figure 3(a). This is because the ocean surface is relatively homogeneous and the aerosol radiative effect is mainly determined by AOD. High values can be found over the tropical Atlantic near the west coasts of northern and central Africa, the Arabian Sea, and near the coasts of anthropogenic aerosol source regions such as East and South Asia.

Over land, both aerosol properties and surface types play important roles in determining the aerosol radiative effect. Figure 7(b) shows large values of radiative effect over the Saharan and Arabian Deserts, where the dust aerosol loading is large (see Figure 3). In these regions, the uncertainty in aerosol retrieval is large as well, so the uncertainty in the estimation of aerosol radiative effect is also large. High values are also seen in East Asia, Eastern Europe and North America, where anthropogenic aerosol emissions are high and the aerosol scattering effect is large. Over land in central Africa, the aerosol radiative effect is small, reflecting the effect of a mixture of scattering and absorbing aerosols. It appears that the importance of this effect also depends on surface type. Over the ocean near the west coast of central Africa, the main aerosol type is also biomass burning. But because of the smaller reflectivity of deep water compared with land surface, the effect of lowering TOA albedo by absorbing aerosols is smaller. Therefore scattering still dominates the net aerosol radiative effect over this part of the tropical Atlantic, and the sign of the forcing is mainly negative. While over the land nearby, because of the higher surface albedo and larger aerosol loading, light absorbing of biomass burning aerosols is much more important, sometimes even causing positive aerosol SWDRE values.

Global mean values of aerosol direct radiative effect are summarized in Table 1, along with aerosol and surface properties. The global mean cloud-free aerosol SWDRE is -4.70 W/m^2 for July 2002. The all-sky value is about one third of the cloud-free value due to cloud cover. The aerosol SWDRE in the northern hemisphere is clearly larger than that in the southern hemisphere. This difference is due mainly to the larger aerosol loading in the northern hemisphere. Continental regions generally have larger aerosol amount in the atmosphere, which may lead to bigger values of aerosol SWDRE. However, compared to ocean surface, the surface reflectance over land is also larger. This may increase the

aerosol absorbing effect and decrease the aerosol scattering effect. So our calculation shows no distinct difference in the cloud-free aerosol direct radiative effect between the ocean and land. However, because the cloud coverage is generally smaller over land than ocean, all-sky aerosol SWDRE is smaller over land.

Table 2 summarizes the global mean values of aerosol direct radiative effect from previous satellite-based studies. These studies calculated the aerosol SWDRE using observed TOA radiative flux from CERES, and the AOD data from MODIS or VIRS. Due to aerosol retrieval issues over land for both nadir-only-viewing MODIS and VIRS, these estimates are limited to only over the ocean. Global mean values of aerosol SWDRE over ocean from this study are also shown for comparison. The results are well within the range of values from these previous studies. The differences can be partly attributed to seasonal and inter-annual variability and differences in cloud screening methods.

Figure 8 shows the relationships between the calculated monthly mean aerosol SWDRE and the MISR 0.56 μm AOD for all 10°×5° regions, over ocean (a) and over land (b). The aerosol SWDRE and AOD are strongly correlated when the AOD is larger than 0.2. When the AOD is smaller, there is less information about aerosol microphysical properties in the MISR radiances, and the retrieved particle property information is less accurate (e.g., Kahn et al., 2001; Kalashnikova and Kahn, 2006). So the points in Figure 8(a) are more dispersed when the AOD is small. The slope in this plot, which represents the radiative effect of aerosols per unit optical depth, is about -31 W/m^2, a value close to that reported for tropical oceans by Loeb and Kato (2002). Over land we see more scatter due to the larger surface heterogeneity. But a trend can be seen in that, with the increase of BHRPAR, the aerosol direct radiative effect tends to be smaller. This is consistent with

the relationships between TOA albedo and AOD for individual BHRPAR bins, as shown in Figure 6.

3.4. Uncertainty discussion

Cloud contamination is an important source of uncertainty in estimating the aerosol direct radiative effect from satellite observations. In this study, we used MISR SVM cloud confidence levels to derive a cloud mask. To reduce cloud contamination, we assume a 17.6×17.6 km^2 area is 'cloudy' if the SVM cloud confidence level in any 1.1×1.1 km^2 pixel within the area is 'likely' or 'very likely'. To test whether this cloud mask is able to filter out most clouds, we did another simulation using a more conservative cloud mask, in which a 17.6×17.6 km^2 area is considered 'cloudy' if the SVM cloud confidence level in any 1.1×1.1 km^2 pixel within this area and the eight neighboring areas is 'likely' or 'very likely'. The results show no significant difference between these two simulations. So we believe most cloud contamination has been filtered out by using the current cloud mask.

MISR is able to retrieve aerosol properties over a variety of terrains, and good correlation between MISR-retrieved AOD and those from Aerosol Robotic Network (AERONET) has been found over southern Africa (Diner et al., 2001), desert areas (Martonchik et al., 2004), and for a range of land and water surfaces around the globe (Abdou et al., 2005; Kahn et al., 2005). For example, by comparing a 2-year measurement record of globally distributed AERONET Sun photometers, Kahn et al. (2005) showed about 2/3 of the MISR-retrieved AOD values fall within [0.05 or 20%×AOD] of AERONET. However, uncertainties in these retrievals are still present, particularly over desert regions, where

surface reflectance is high, and over remote oceans, where aerosol loading is typically very low. The impact of large uncertainty in aerosol retrieval over remote oceans on the calculated global mean aerosol SWDRE is expected to be small, because the radiative effect in these regions is small due to the low aerosol loading. Over brighter desert or other land surface, the MISR-retrieved AOD using current algorithm is usually skewed high (Kahn et al., 2005), which may lead to an overestimation of $\alpha_{\text{no aerosol}}$ and underestimation of aerosol SWDRE.

Another source of uncertainty is in the calculation of TOA albedo. This calculation consists of two steps: the radiance-to-flux conversion and the spectral-to-broadband conversion. In the first step, top-leaving BRFs were integrated either using an azimuthal model (AZM) or a Solid Angle Weighting method for cloud-free scenes. There are uncertainties in determining the integration coefficients for either method (Diner et al., 1999a). The standard deviation of the albedo values with the AZM approach has been evaluated for different surface types in cloud-free scenes. Most albedo errors lie between 1% and 2% (where a 1% error indicates an absolute albedo error of 0.01) (Diner et al., 1999a; Sun et al., 2006). By comparing MISR-derived albedos with those measured by CERES, the spectral-to-broadband conversion leads to errors in the MISR results of about 2.0% (Loeb et el., 2006). The RMS difference between MISR and CERES albedos due to both radiance-to-flux conversion and the spectral-to-broadband conversion is thus estimated to be ~4.3% (Sun et el., 2006). However, the uncertainty analysis of Sun et al. (2006) was limited to overcast ocean scenes. Further studies are needed to evaluate the uncertainty of TOA broadband albedo over land, as well as the clear scene over ocean.

Since Terra crosses the equator on the day side of each orbit at around 10:30am local time, the monthly mean aerosol SWDRE values we calculated are actually mean values

for about this time of day. Both surface reflectivity and aerosol loading have diurnal variations, for example over urban areas and wildfire regions. Loeb and Manalo-Smith (2005) used diurnal albedo models from CERES TRMM measurements to calculate daily mean albedo over the tropical ocean. Not enough information is available to construct a global diurnal albedo model over both ocean and land from the data used here. The effects from the biomass burning diurnal variation on aerosol distribution and global climate are being studied using a chemical transport model with updated biomass burning emission inventory that includes diurnal cycle (Chen et al., in preparation).

3.5. Use of SVM scene classifiers to separate radiative effect due to different aerosol types

The radiative effect calculated above is from all aerosols. As shown in previous studies, different aerosol types have different effects on TOA albedo, and hence, the radiative balance of the atmosphere. It is desirable to separate the radiative effects due to different aerosol types. MISR SVM scene classifiers not only differentiate cloudy pixels, but also report whether the aerosol is likely smoke or dust when the pixel is labeled as 'aerosol'. This suggests the possibility of using SVM scene classifiers to estimate the aerosol radiative effect due to different aerosol types.

We conducted a test simulation to calculate the smoke aerosol radiative effect in North America for July 2002. We calculated the mean TOA albedo for pixels classified as 'smoke aerosols' and for pixels classified as 'clear (no aerosol)'. The smoke aerosol radiative effect is calculated based on the difference of these two albedos and the fraction of pixels labeled as 'smoke aerosol'.

Although the SWDRE from smoke aerosols is affected by many factors such as smoke emissions, smoke transport, removal processes, surface types, solar radiation, etc., we expect larger SWDRE values near fire source regions. As shown in Figure 9, the cloud-free SWDRE from smoke aerosols calculated from the SVM scene classifiers matches the pattern of wild fires recorded by the MODIS Rapid Response System (http://rapidfire.sci.gsfc.nasa.gov) and integrated by the Fire Information for Resource Management System (FIRMS) (NASA/University of Maryland, 2002), to a certain extent. However, the uncertainty in such a calculation is large, for several reasons.

First, the SVM scene classification only labels thick visible aerosol layers as 'Aerosol'. The SVM scene classifier was trained by MISR scientists who labeled hundreds of scenes using a custom interactive tool. However, the threshold for differentiating 'Aerosol' and 'Clear' pixels is arbitrary. So those pixels having aerosol loading that is not visible in the MISR images examined were not labeled as 'Aerosol'. Due to this limitation, the total number of the 'smoky' pixels is underestimated.

The albedo for aerosol-free pixels is likely overestimated since many 'Surface' pixels actually have some aerosol loading. This may reduce the difference of albedo values for 'Smoke' pixels and 'Surface' pixels, thereby leading to the underestimation of SWDRE from smoke aerosols.

In addition, the current SVM scene classifier data is only at a provisional level of maturity. The overall accuracy of the 5-type classifier was found to be 80.9% (Mazzoni et al., 2006). However, the current SVM has been tuned to detect as many aerosols as possible, thus leading to many false positives compared to human expert selections (Mazzoni et al., 2006). For a pixel that is labeled 'Aerosol', there is a 35% probability that it is actually 'Cloud', and a 15% chance that it is actually 'Surface', either 'Land' or

'Water'. In addition, the SVM scene classification differentiates smoke and dust poorly. Mazzoni et al. (2006) reported that the aerosol sub-classification validation has not yet been completed.

For the above reasons, we chose not to use the SVM scene classifiers in the calculation of global aerosol radiative effect presented here. It would be a promising approach with improved SVM classification.

4. Conclusions

The multi-angle, multi-spectral MISR data make it possible to retrieve aerosol properties as well as optical depth over land and ocean. In this study, global MISR observations were used to estimate the shortwave direct radiative effect of aerosols on a global scale.

Good correlations between MISR-derived TOA broadband albedo and 0.56 μm AOD were found for most 10°×5° regions. The change of TOA albedo per unit AOD is different in different regions, reflecting spatial variations in aerosol properties and surface types. Over the ocean and most regions over land, increased AOD correlates with increased TOA albedo, as expected from the scattering contributions of bright aerosols. But in biomass burning regions where absorbing aerosol loading is high, the aerosol effect on TOA albedo is small due to the competing effect of light absorption by darker aerosols.

We divided the land surface into 26 bins according to their MISR-retrieved BHRPAR values. In non-absorbing aerosol dominant regions, the slope of AOD-TOA albedo decreases as BHRPAR increases, which indicates that the aerosol scattering effect on TOA albedo is smaller over brighter surfaces, as might be expected. In high BHRPAR

regions such as the Saharan desert, the correlation between TOA albedo and AOD exhibits large dispersion, in part due to larger uncertainty in the aerosol retrievals.

This study demonstrates the decrease of TOA albedo in the presence of more light-absorbing biomass burning aerosols over Central Africa and the nearby Atlantic region. We also observed that this effect is larger over land, where the radiation absorbed by aerosols produces greater contrast with light reflected from surface. For the same reason, in Central Africa, the slope of AOD-TOA albedo for land surface with higher BHRPAR values tends to be smaller. This light absorbing effect can even dominate the aerosol scattering effect, causing positive radiative effect.

The global mean aerosol direct radiative effect for July 2002 is estimated to be -4.7 W/m^2 for cloud-free sky and -1.9 W/m^2 for all sky. The global pattern of aerosol SWDRE is affected by aerosol loading, aerosol properties, and surface type. The Northern Hemisphere shows a larger aerosol direct radiative effect than the Southern Hemisphere, as might be expected. The values obtained in this study are within the range of published aerosol SWDRE values from other satellite-based studies, with the differences among estimates partially due to seasonal and inter-annual variability. The aerosol SWDRE over the ocean alone is not enough to explain all the climate effects caused by aerosol scattering and absorption. High aerosol loadings, particularly those due to the anthropogenic emissions, are generally over the continental land. The land surface is much more heterogeneous than the ocean surface, and there are larger spatial and temporal variations in aerosol concentrations and properties over the land. In this paper, for the first time, we presented an approach of estimating the aerosol SWDRE on a global scale based on satellite observations, over both ocean and land. The advantage in this approach is the use of more reliable aerosol and surface properties from multi-angular

satellite instrument. Compared with the studies only over the ocean, this approach can be used to provide a more thorough representation of the climate effect due to aerosol scattering and absorption.

We also examined the aerosol SWDRE under different aerosol loadings as indicated by 0.56 μm AOD. The radiative effect of aerosols per unit optical depth is about -31 W/m^2 over the ocean. Over land, the aerosol SWDRE per unit aerosol optical depth is smaller, and decreases as the BHRPAR increases.

By examining regional AOD-TOA albedo correlations, and BHRPAR for specific grid boxes, the approach presented in this paper quantifies global aerosol direct radiative effect due to scattering and absorption, over both ocean and land. Although current MISR SVM classifiers have not provided satisfactory results, this approach can be extended to examine the radiative effect due to particular aerosol species once we have more information. Aerosol effects on a particular region may be very different during different seasons and different years. So we also plan to extend the approach presented here to include seasonal and inter-annual variability. With a more extensive data set, the uncertainties in AOD-TOA albedo regressions will likely be reduced. In addition, diurnal quantification of aerosol direct radiative effect will also be included in the future, though this will require data sets in addition to MISR.

Acknowledgments

This work is performed at the Jet Propulsion Laboratory, California Institute of Technology, under contract with NASA. The research of Y. Chen is funded in part by the NASA Earth Observing System MISR project, and in part by NASA grant # 622-59-66-

40. Q. Li is supported in part by the Atmospheric Composition Modeling and Analysis program. The work of R. Kahn is funded in part by the NASA Earth Sciences Climate & Radiation and Atmospheric Composition programs, under H. Maring and P. DeCola, respectively, and in part by the MISR project. MISR data were obtained from the NASA Langley Atmospheric Sciences Data Center (http://www.eosweb.larc.nasa.gov).

References

Abdou, W.A., D.J. Diner, J.V. Martonchik, C.J. Bruegge, R.A. Kahn, B.J. Gaitley, K.A. Crean, L.A. Remer, and B. Holben, 2005: Comparison of coincident MISR and MODIS aerosol optical depths over land and ocean scenes containing AERONET sites. *J. Gelphys. Res*., **110**, D10S07, doi:10.1029/2004JD004693.

Ackerman, A.S., O.B. Toon, D.E. Stevens, A.J. Heymsfield, V. Ramanathan, and E.J. Welton, 2000: Reduction of tropical cloudiness by soot. *Science*, **288**, 1042-1047.

Armston, J. D., P.F. Scarth, S.R. Phinna, and T.J. Danaher, 2007: Analysis of multi-date MISR measurements for forest and woodland communities, Queensland, Australia. *Rem. Sens. Environ.*, **107**, 287-298.

Bellouin, B., O. Boucher, J. Haywood, and M.S. Reddy, 2005: Global estimates of aerosol direct radiative forcing from satellite measurements. *Nature*, **438**, 1138-1140, doi:10.1038/nature04348.

Bull, M., J. Matthews, C. Moroney, and M. Smyth, 2005: Data products specifications, Rep. D13963, Rev. N, Jet. Propul. Lab., Pasadena, California.

Charlson, R.J., J. Langner, and H. Rodhe, 1990: Sulphate aerosol and climate. *Nature*, **348**, 22.

Chen, W-T., R. Kahn, W-H. Li, and J. Seinfeld, 2007: Sensitivity of multi-angle imaging to optical and microphysical properties of biomass burning particles. *J. Geophys. Res.,* submitted.

Christopher, S.A., J. Chou, J. Zhang, X. Li, T.A. Berendes and R.M. Welch, 2000: Shortwave direct radiative forcing of biomass burning aerosols estimated using VIRS and CERES data. *Geophys. Res. Lett.*, **27**, 2197-2200.

Christopher, S.A., and J. Zhang, 2002: Shortwave aerosol radiative forcing from MODIS and CERES observations over the oceans. *Geophys. Res. Lett.*, **29**, 1859, doi: 10.1029/2002GL014803.

Coakley Jr., J.A., R.D. Cess, and F.B. Yurevich, 1983: The effect of tropospheric aerosols on the earth's radiation budget: A parameterization for climate models. *J. Atmos. Sci.*, **40**, 116-138.

Diner, D.J., J.C. Beckert, T.H. Reilly, C.J. Bruegge, J.E. Conel, R. Kahn, J.V. Martonchik, T.P. Ackerman, R. Davies, S.A.W. Gerstl, H.R. Gordon, J-P. Muller, R. Myneni, R.J. Sellers, B. Pinty, and M.M. Verstraete, 1998: Multi-angle Imaging SpectroRadiometer (MISR) description and experiment overview. *IEEE Trans. Geosci. Rem. Sens.*, **36** (4), 1072-1087.

Diner, D.J., R. Davies, T. Varnai, C. Moroney, C. Borel, S.A.W. Gerstl, and D.L. Nelson, 1999a: MISR level 2 top-of-atmosphere albedo algorithm theoretical basis. Rep. D13401, Rev. D, Jet. Propul. Lab., Pasadena, California.

Diner, D.J., J.V. Martonchik, C. Borel, S.A.W. Gerstl, H.R. Gordon, Y. Knyazikhin, B., and M.M. Verstraete, 1999b: MISR level 2 surface retrieval algorithm theoretical basis. Rep. D11401, Rev. D, Jet. Propul. Lab., Pasadena, California.

Diner, D.J., W.A. Abdou, T.P. Ackerman, K. Crean, H.R. Gordon, R.A. Kahn, J.V. Martonchik, S. McMuldroch, S.R. Paradise, B. Pinty, M.M. Verstraete, M. Wang, and

R.A. West, 2001a: MISR level 2 aerosol retrieval algorithm theoretical basis. Rep. D11400, Rev. E, Jet. Propul. Lab., Pasadena, California.

Diner, D.J., W.A. Abdou, J.E. Conel, K.A. Crean, B.J. Gaitley, M.Helmlinger, R.A. Kahn, J.V. Martonchik, and S.H. Pilorz, 2001b: MISR aerosol optical depth retrievals over southern Africa during the SAFARI-2000 dry season campaign. *Geophys. Res. Lett.*, **28**, 3127-3130.

Diner D.J., B.H. Braswell, R. Davies, N. Gobron, J. Hu, Y. Jin, R.A. Kahn, Y. Knyazikhin, N. Loeb, J.-P. Muller, A.W. Nolin, B. Pinty, C.B. Schaaf, G. Seiz and J. Stroeve, 2005: The value of multiangle measurements for retrieving structurally and radiatively consistent properties of clouds, aerosols, and surfaces. *Remote Sensing of Environment*, **97**, 495-518.

Hansen, J., M. Sato, A. Lacis, R. Ruedy, I. Tegen, and E. Matthews, 1998: Climate forcings in the Industrial era. *Proc. Natl. Acad. Sci.*, **95**, 12,753-12,758

Hu, J., Y. Su, B. Tan, D. Huang, W. Yang, M. Schull, M.A. Bull, J.V. martonchik, D.J. Diner, and Y. Knyazikhin, 2007: Analysis of the MISR LAI/FPAR product for spatial and temporal coverage, accuracy and consistency. *Rem. Sens. Environ.*, **107**, 334-347.

IPCC (Intergovernmental Panel on Climate Change), 2001: In Houghton J.T. et al., (Eds.), Climate change 2001, Cambridge University Press, 878.

Kahn, R., B. Gaitley, J. Martonchik, D. Diner, K. Crean, and B. Holben, 2005: MISR global aerosol optical depth validation based on two years of coincident AERONET observations. *J. Geophys. Res.,* **110**, D10S04, doi:10:1029/2004JD004706.

Kahn, R., P. Banerjee, and D. McDonald, 2001: The Sensitivity of Multiangle Imaging to Natural Mixtures of Aerosols Over Ocean. *J. Geophys. Res.,* **106**, 18219-18238.

Kalashnikova, O.V. and R.A. Kahn, 2006: The ability of multi-angle remote sensing observations to identify and distinguish mineral dust types: Part 2. Sensitivity data analysis. *J. Geophys. Res.*, **111**, D11207, doi:10.1029/2005JD006756.

Kaufman, Y., D. Tanre, and O. Boucher, 2002: A satellite view of aerosols in the climate system. *Nature*, **419**, 215-223.

Kinne, S., M. Schulz, C. Textor, S. Guibert, Y. Balkanski, S. E. Bauer, T. Berntsen, T. F. Berglen, O. Boucher, M. Chin, W. Collins, F. Dentener, T. Diehl, R. Easter, J. Feichter, D. Fillmore, S. Ghan, P. Ginoux, S. Gong, A. Grini, J. Hendricks, M. Herzog, L. Horowitz, I. Isaksen, T. Iversen, A. Kirkevag, S. Kloster, D. Koch, J. E. Kristjansson, M. Krol, A. Lauer, J. F. Lamarque, G. Lesins, X. Liu, U. Lohmann, V. Montanaro, G. Myhre, J. Penner, G. Pitari, S. Reddy, O. Seland, P. Stier, T. Takemura, and X. Tie, 2006: An AeroCom initial assessment – optical properties in aerosol component modules of global models. *Atmos. Chem. Phys.*, **6**, 1815-1834.

Liang, S., A.H. Strahler, and C. Walthall, 1999: Retrieval of land surface albedo from satellite observations: A simulation study. *J. Appl. Meteor.*, **38**, 712-725.

Loeb, N.G., and S. Kato, 2002: Top-of-atmosphere direct radiative effect of aerosols over the tropical oceans from the Clouds and the Earth's Radiant Energy System (CERES) satellite instrument. *J. Climate*, **15**, 1474-1484.

Loeb, N.G., and N. Manalo-Smith, 2005: Top-of-atmosphere direct radiative effect of aerosols over global oceans from merged CERES and MODIS observations. *J. Climate*, **18**, 3506-3526.

Martonchik, J.V., D.J. Diner, B. Pinty, M.M. Verstraete, R.B. Myneni, Y. Knyazikhin, and H.R. Gordon, 1998: Determination of land and ocean reflective, radiative, and

biophysical properties using multiangle imaging. *IEEE Trans. Geosci. Remote Sens.*, **36**, 1266-1281.

Martonchik, J.V., D.J. Diner, K.A. Crean and M.A. Bull, 2002: Regional Aerosol Retrieval Results From MISR. IEEE Trans. Geosci. *Remote Sens.*, **40**, 1520-1531.

Martonchik, J.V., D.J. Diver, R. Kahn, and B. Gaitley, 2004: Comparison of MISR and AERONET aerosol optical depths over desert sites. *Geophys. Res. Lett.*, **31**, L16102, doi: 10.1029/2004GL019807.

Mazzoni, D., M. Garay, R. Davies, and D. Nelson, 2007: An operational MISR pixel classifier using Support Vector Machines, *Rem. Sens. Env*. 107, 149-158.

Menon, S., J. Hansen, L. Nazarenko, and Y. Luo, 2002: Climate Effects of Black Carbon Aerosols in China and India. *Science*, **297**, 2250-2253, DOI: 10.1126/science.1075159.

NASA/University of Maryland, 2002: MODIS Hotspot / Active Fire Detections. Data set. MODIS Rapid Response Project, NASA/GSFC [producer], University of Maryland, Fire Information for Resource Management System [distributors]. Available on-line [http://maps.geog.umd.edu].

Remer, L. A. and Y.J. Kaufman, 2006: Aerosol direct radiative effect at the top of the atmosphere over cloud free ocean derived from five years of MODIS data. *Atmos. Chem. Phys.*, **6**, 237–253.

Rudnick, D. L., R.A. Weller, C.C. Eriksen, T.D. Dickey, J. Marra, and C. Langdon, 1997: Moored instruments weather Arabian Sea monsoons, yield data. *Eos, Trans. Amer. Geophys. Union*, **78**, 117, 120-121.

Sun, W., N.G. Loeb, R. Davies, K. Loukachine, and W.F. Miller, 2006: Comparison of MISR and CERES top-of-atmosphere albedo. *Geophys. Res. Lett.*, **33**, L23810, doi: 10.1029/2006GL027958.

Wielicki, B. A., B.R. Barkstrom, E.F. Harrison, R.B. Lee III, G.L. Smith, and J.E. Cooper, 1996: Clouds and Earth's Radiant Energy System (CERES): An earth observing system experiment. *Bull. Amer. Meteor. Soc.*, **77**, 853-868.

Yu, H., R.E. Dickinson, M. Chin, Y.J. Kaufman, M. Zhou, Y. Tian, O. Dubovik, and B.N. Holben, 2004: The direct radiative effect of aerosols as determined from a combination of MODIS retrievals and GOCART simulations. *J. Geophys. Res.*, **109**, D03206, doi:10.1029/2003JD003914.

Yu, H., Y.J. Kaufman, M. Chin, G. Feingold, L.A. Remer, T.L. Anderson, Y. Balkanski, N. Bellouin, O. Boucher, S. Christopher, P. DeCola, R. Kahn, D. Koch, N. Loeb, M.S. Reddy, M. Schulz, T. Takemura, and M. Zhou, 2006: A review of measurement-based assessments of the aerosol direct radiative effect and forcing. *Atmos. Chem. Phys.*, **6**, 613-666.

Zhang, J., and S.A. Christopher, 2005: Shortwave aerosol radiative forcing over cloud-free oceans from Terra: 2. Seasonal and global distributions. *J. Geophys. Res.*, **110**, D10S24, doi: 10.1029/2004JD005009.

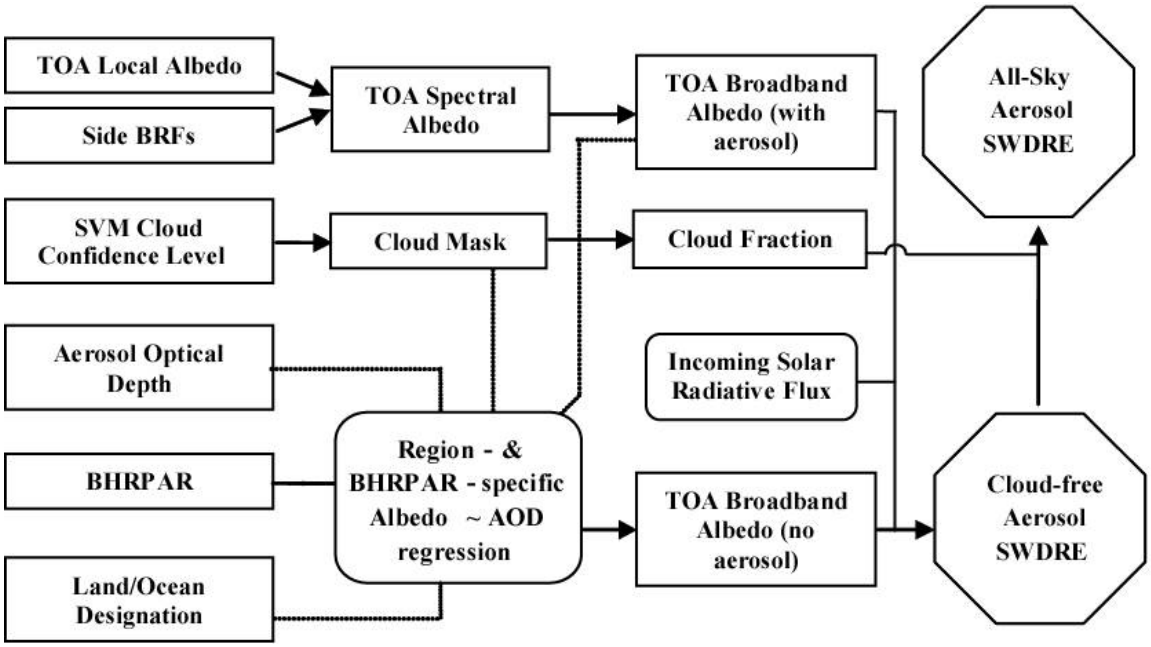

Figure 1. Schematic flowchart of the aerosol SWDRE calculation presented in this study.

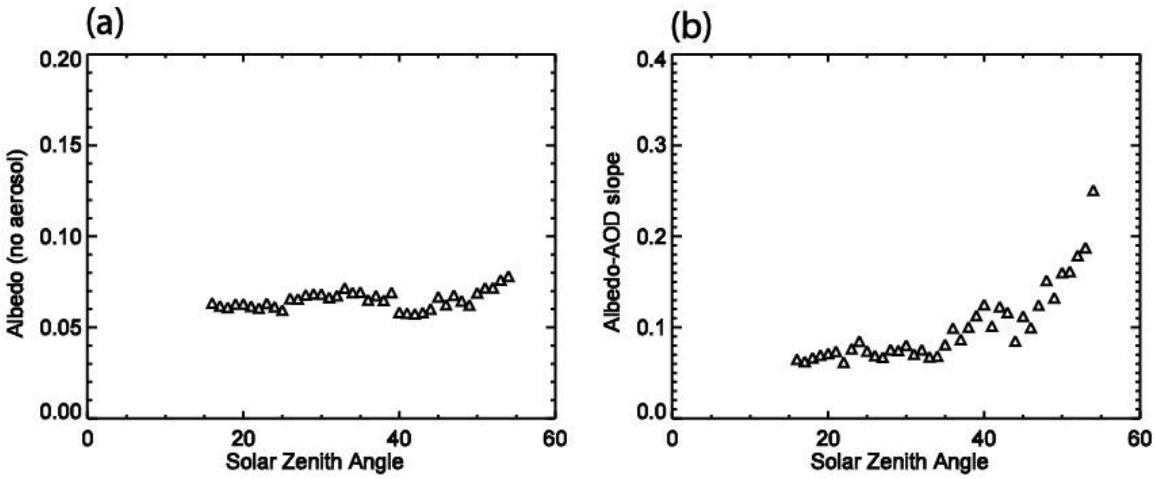

Figure 2. Intercept (a) and slope (b) of MISR TOA broadband albedo against 0.56 μm AOD as functions of solar zenith angle over ocean for July 2002.

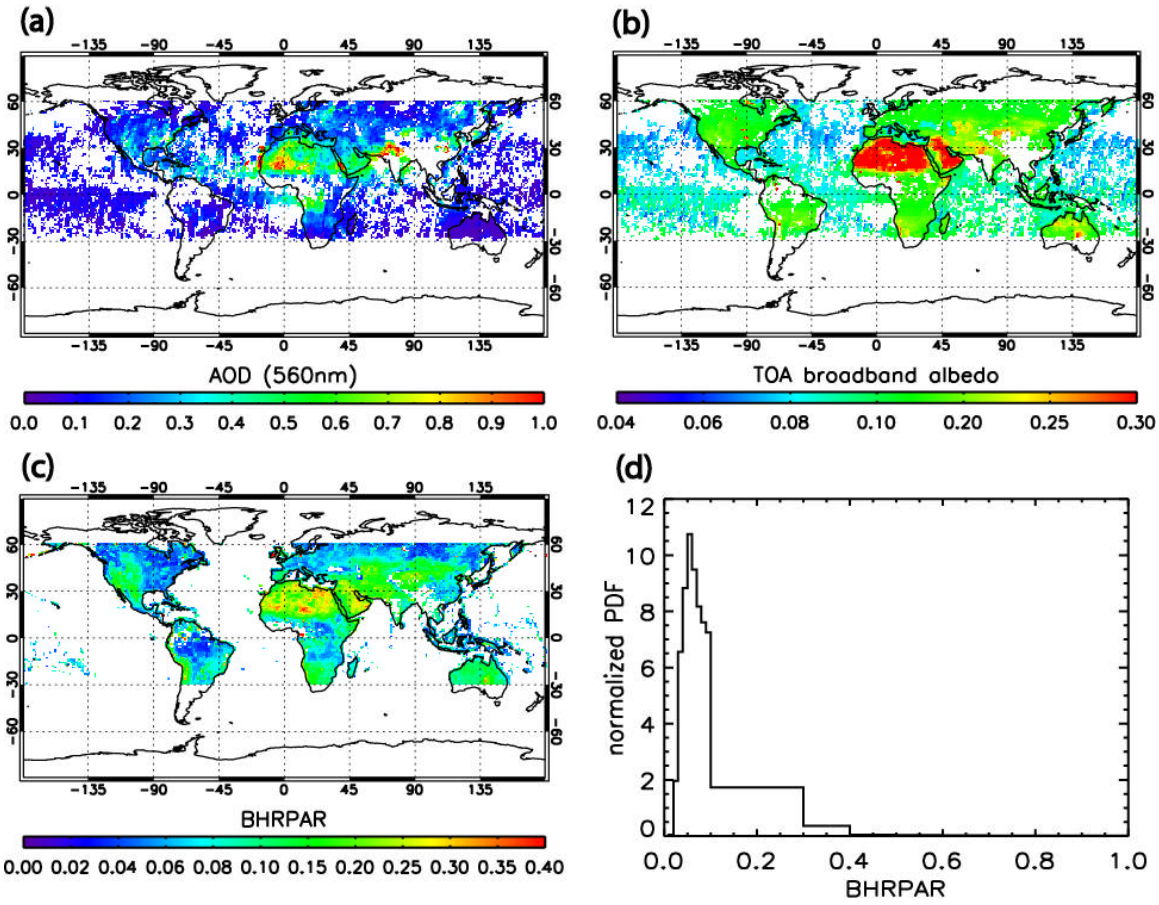

Figure 3. Global distributions of MISR (a) 0.56 μm AOD; (b) cloud-free TOA albedo; (c) BHRPAR for July 2002. Probability distribution of BHRPAR is also shown (d).

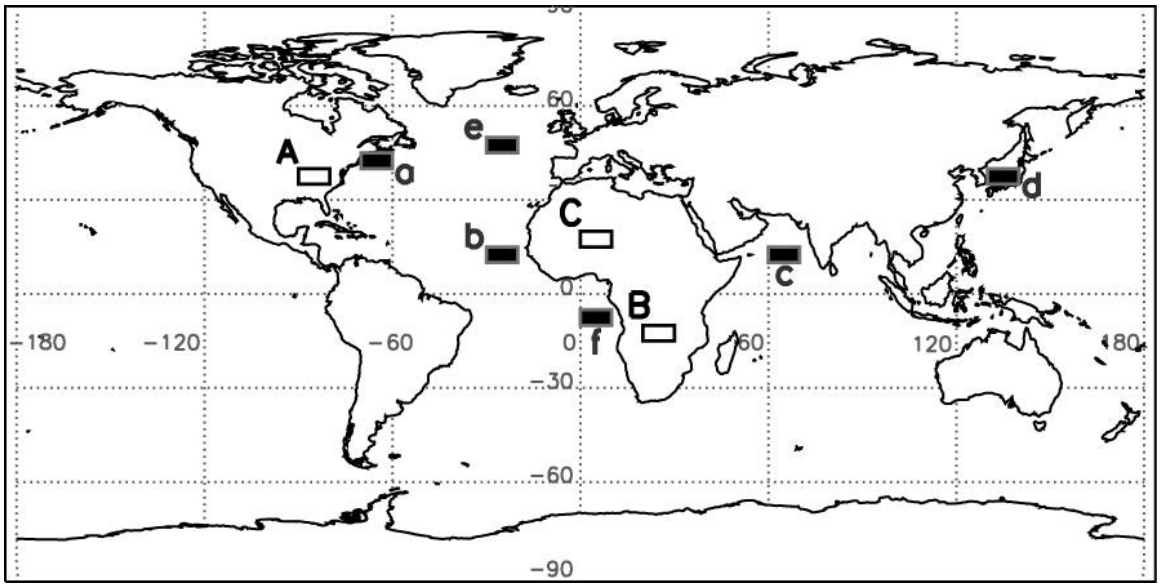

Figure 4. Locations of oceanic regions (a-f) and land regions (A-C) that are chosen for illustrating MISR TOA albedo and AOD regressions.

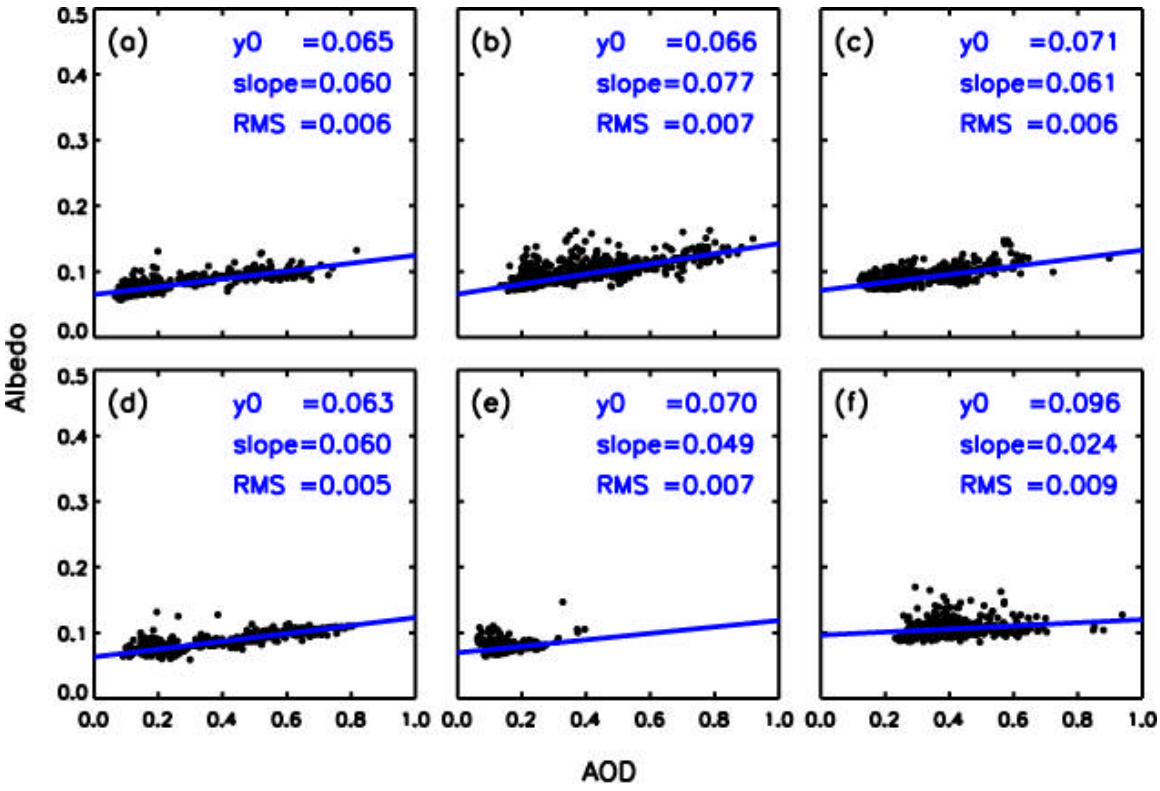

Figure 5. Relationships between MISR TOA broadband albedo and 0.56 μm AOD over representative oceanic regions: (a) East US Coast; (b) West Africa Coast; (c) Arabian Sea; (d) East Asia Coast; (e) North Atlantic; (f) Central Africa Coast. Regression lines, as well as the slope, intercept, and RMS are also shown if the regression is successful.

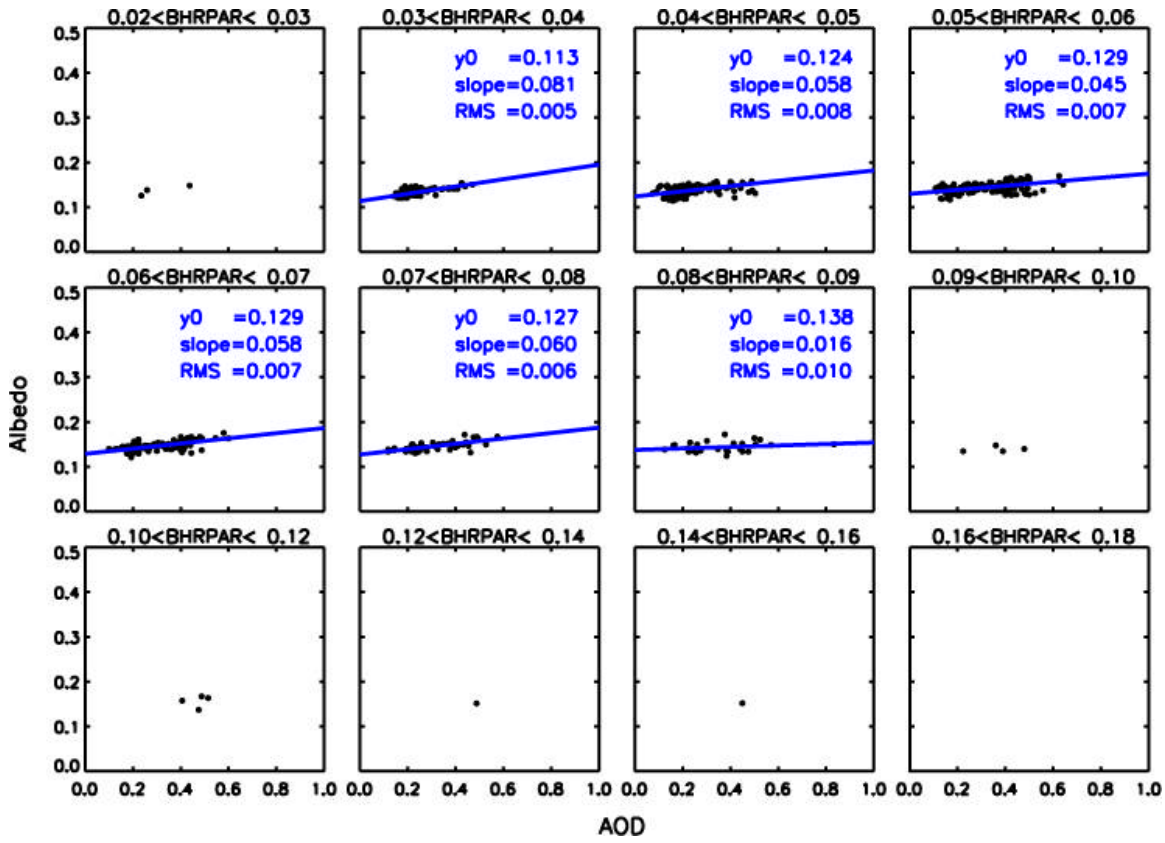

Figure 6(a). Relationships between TOA albedo and 0.56 μm AOD over a representative land region (region (A) as shown in Figure 4), stratified by BHRPAR.

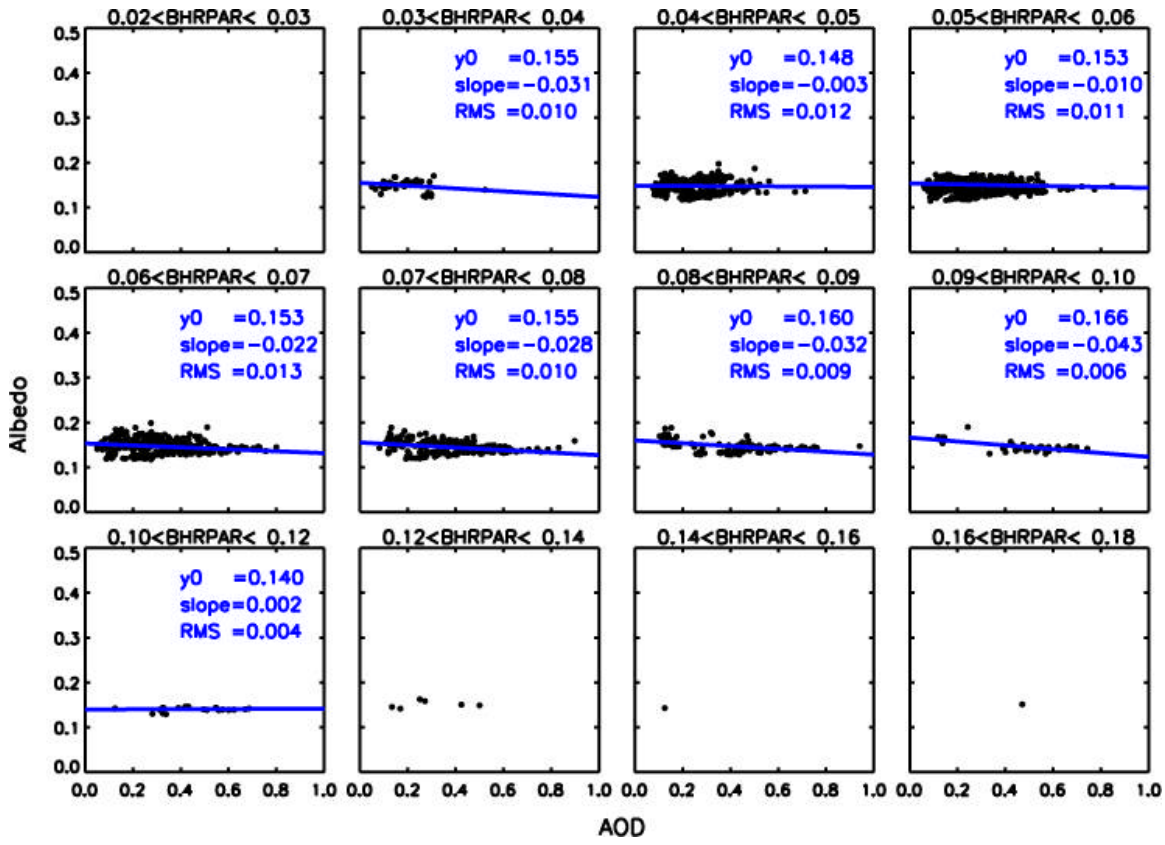

Figure 6(b). Same as Fig. 6(a), but for region (B) as shown in Fig. 4.

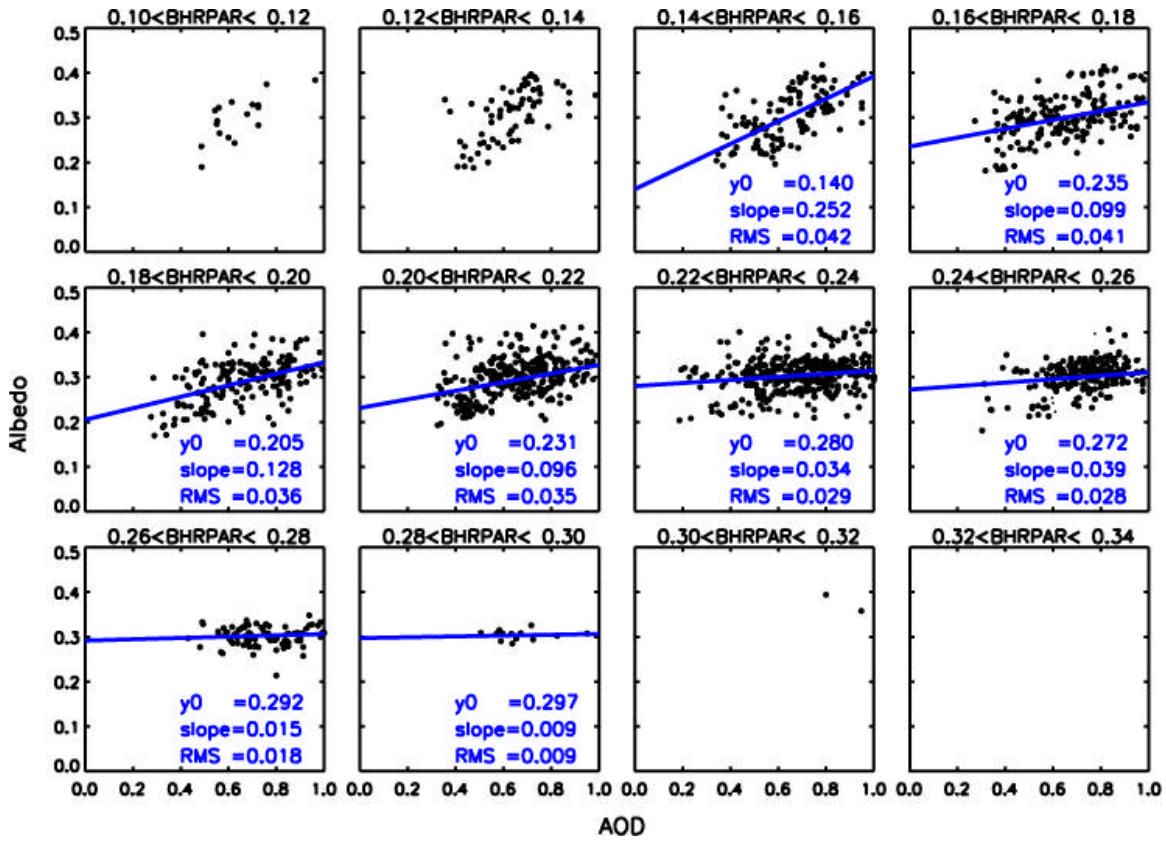

Figure 6(c). Same as Fig. 6(a), but for region (C) as shown in Fig. 4.

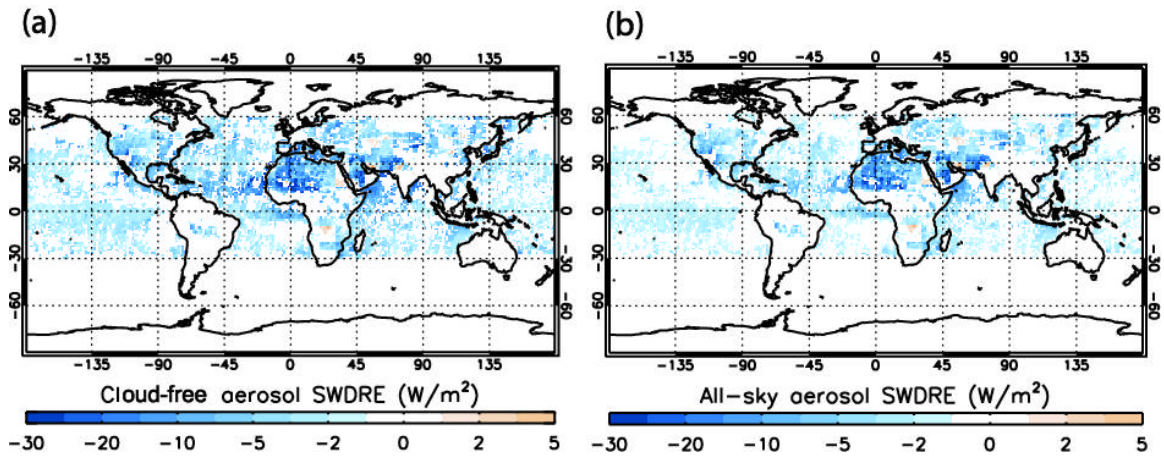

Figure 7. (a) Cloud-free and (b) all-sky aerosol shortwave direct radiative effect (W/m^2) for July 2002 from this study.

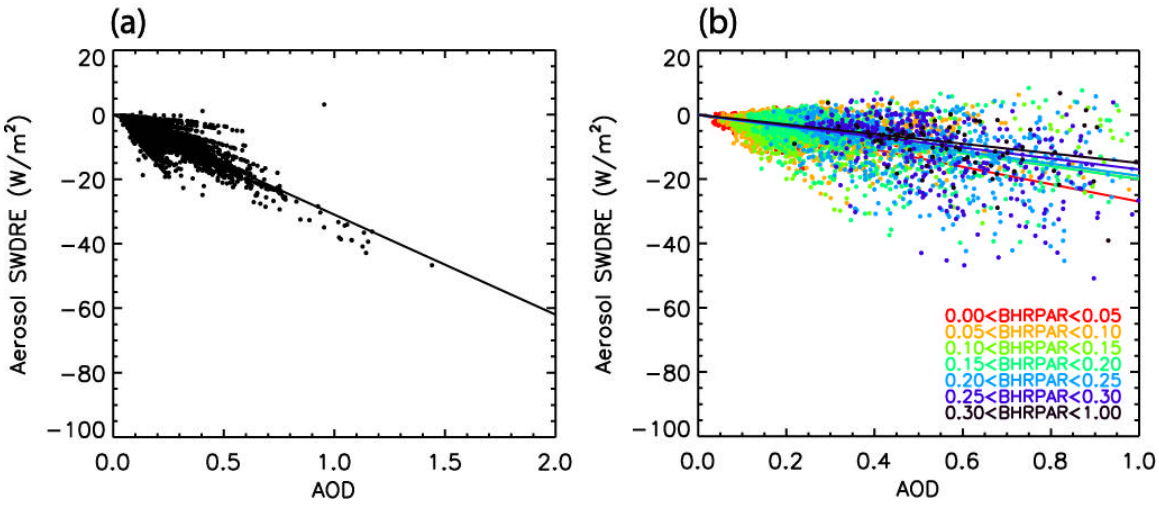

Figure 8. Aerosol SWDRE plotted against 0.56 μm AOD (a) over ocean and (b) over land for different BHRPAR values.

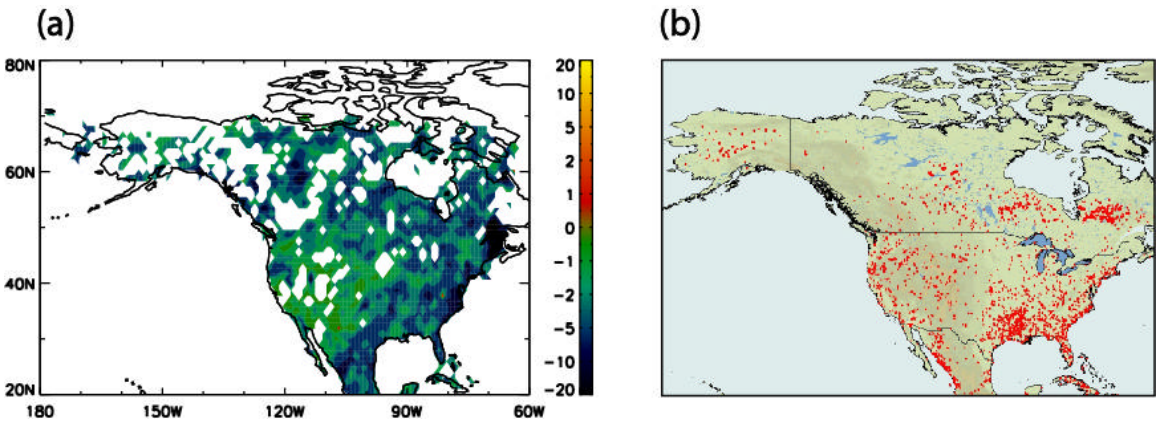

Figure 9. (a) Cloud-free aerosol SWDRE from smoke aerosols in Northern America for July 2002 calculated using MISR SVM scene classifiers. (b) MODIS wild fire occurrence from Fire Information for Resource Management System (FIRMS) for July 2002.

Table 1. Global mean values of aerosol SWDRE, AOD and BHRPAR for July 2002.

	AOD	BHRPAR	Aerosol SWDRE (Cloud-free) (W/m^2)	Aerosol SWDRE (All-sky) (W/m^2)
Global	0.19	0.040	-4.70	-1.49
NH	0.25	0.048	-5.71	-3.86
SH	0.13	0.026	-2.98	-1.86
Ocean	0.19	–	-4.54	-1.95
Land	0.28	0.040	-4.88	-1.18

Table 2. Aerosol SWDRE calculated using satellite observations in the literature and from this study.

Source	Aerosol SWDRE (W/m^2)	Spatial coverage	Temporal coverage	Satellite data source
Zhang and Christopher, 2005	-6.4 ± 2.6	Cloud-free oceans	09/2000-08/2001	CERES, MODIS
Christopher and Zhang, 2002	-6	Cloud-free oceans	09/2000	CERES, MODIS
Loeb and Kato, 2002	-4.6 ± 1	Cloud-free tropical oceans	01/1998-08/1998, 03/2000	CERES, TRMM VIRS
Loeb and Manalo-Smith, 2005	-5.5, -3.8*	Cloud-free oceans	03/2000-12/2003	CERES, MODIS
	-2.0, -1.6*	All-sky oceans		
This study	-4.5	Cloud-free oceans	07/2002	MISR
	-2.0	All-sky oceans		

*: using two different cloud masks.